

© 2019 by Akshat Puri. All rights reserved.

MEASUREMENT OF ANGULAR AND MOMENTUM DISTRIBUTIONS OF CHARGED  
PARTICLES WITHIN AND AROUND JETS IN Pb+Pb AND  $p\bar{p}$  COLLISIONS AT  
 $\sqrt{S_{NN}} = 5.02$  TeV WITH ATLAS AT THE LHC

BY  
AKSHAT PURI

DISSERTATION

Submitted in partial fulfillment of the requirements  
for the degree of Doctor of Philosophy in Physics  
in the Graduate College of the  
University of Illinois at Urbana-Champaign, 2019

Urbana, Illinois

Doctoral Committee:

Professor Matthias Grosse Perdekamp, Chair  
Professor Anne Marie Sickles, Advisor  
<sup>1</sup> Professor Aida El-Khadra  
Professor Bryce Gadaway

# Abstract

<sup>2</sup> Studies of the fragmentation of jets into charged particles in heavy-ion collisions can help in understanding  
<sup>3</sup> the mechanism of jet quenching by the hot and dense matter created in such collisions, the quark-gluon  
<sup>4</sup> plasma. This thesis presents a measurement of the angular distribution of charged particles around the jet  
<sup>5</sup> axis as measured in Pb+Pb and  $pp$  collisions collided at a center of mass energy of  $\sqrt{s_{NN}} = 5.02$  TeV. The  
<sup>6</sup> measurement is done using the ATLAS detector at the Large Hadron Collider, and utilizes  $0.49 \text{ pb}^{-1}$  of  
<sup>7</sup> Pb+Pb and  $25 \text{ pb}^{-1}$  of  $pp$  data collected in 2015. The measurement is performed for jets reconstructed  
<sup>8</sup> with the anti- $k_t$  algorithm with radius parameter  $R = 0.4$ , and is extended to regions outside the jet cone.  
<sup>9</sup> Results are presented as a function of Pb+Pb collision centrality, and both jet and charged-particle transverse  
<sup>10</sup> momenta. It was observed that in Pb+Pb collisions there is a broadening of the jet for charged particles with  
<sup>11</sup>  $p_T < 4 \text{ GeV}$ , along with a narrowing for charged particles with  $p_T > 4 \text{ GeV}$ . Ratios between the angular  
<sup>12</sup> distributions in Pb+Pb and  $pp$  showed an enhancement for particles with  $p_T < 4 \text{ GeV}$  in Pb+Pb collisions,  
<sup>13</sup> with the enhancement increasing up to 2 for  $r < 0.3$ , and remaining constant for  $0.3 < r < 0.6$ . Charged  
<sup>14</sup> particles with  $p_T > 4 \text{ GeV}$  show a small enhancement in the jet core for  $r < 0.05$ , with a growing suppression  
<sup>15</sup> of up to 0.5 for  $r < 0.3$  in Pb+Pb collisions. The depletion remains constant for  $0.3 < r < 0.6$ .

*For my Mother, Father, and Brother*

# Contents

18	<b>Chapter 1 Theoretical Introduction</b>	<b>1</b>
19	1.1 Quantum Chromodynamics	1
20	1.2 Heavy Ion Collisions and the Quark Gluon Plasma	4
21	1.2.1 Heavy Ion Collisions	4
22	1.2.2 The Quark Gluon Plasma	9
23	1.3 Jets and Jet Quenching	11
24		
25	<b>Chapter 2 Major Jet Measurements</b>	<b>16</b>
26	2.1 Jet Reconstruction	16
27	2.2 Modification of jet yields: Jet $R_{AA}$	18
28	2.3 Jet $X_J$	18
29	2.4 Jet Fragmentation	18

# Chapter 1

## Theoretical Introduction

This section shall discuss the theoretical background necessary to understand jet measurements. It will discuss the fundamentals of quantum chromodynamics (QCD), the heavy ion collision system and the quark gluon plasma that is formed, and finally jets and jet energy loss.

### 1.1 Quantum Chromodynamics

Quantum Chromodynamics is a gauge theory with SU(3) symmetry that describes the dynamics of the strong interactions between quarks and gluons. It is part of the Standard Model [1], the building blocks of which are shown in Figure 1.1.

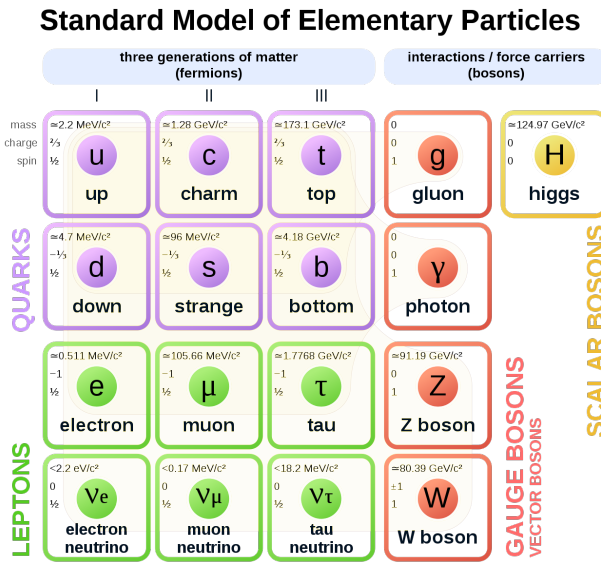


Figure 1.1: The elementary particles of the standard model.

Quarks are fermions with a spin of 1/2, and carry a fractional electric charge as well as a color charge. They all have mass and come in six flavors: up, down, top, bottom, strange, charm. The lightest quarks

<sup>39</sup> (u and d) combine and form stable particles, while the heavier quarks can only be produced in energetic  
<sup>40</sup> environments and decay rapidly. Gluons are gauge bosons (force carriers) with a spin of 1, and are what hold  
<sup>41</sup> quarks together. The dynamics of the quarks and gluons are described by the QCD Lagrangian given as [2]:

$$\mathcal{L}_{\text{QCD}} = \sum_q \bar{\psi}_{q,a} (i\gamma^\mu \partial_\mu \delta_{ab} - g_s \gamma^\mu t_{ab}^C \mathcal{A}_\mu^C - m_q \delta_{ab}) \psi_{q,b} - \frac{1}{4} F_{\mu\nu}^A F^{A\mu\nu} \quad (1.1)$$

<sup>42</sup> where  $\psi_{q,a}$  and  $\psi_{q,b}$  are quark-filled spinors for a quarks with flavor  $q$ , mass  $m_q$ , and color  $a$  and  $b$  respectively,  
<sup>43</sup> with the values for  $a$  and  $b$  ranging from 1 to 3 (for the three colors). The  $\mathcal{A}_\mu^C$  corresponds to the gluon field  
<sup>44</sup> with  $C$  taking values from 1 through 8 (for the 8 types of gluons). The  $t_{ab}^C$  corresponds to the Gell-Mann  
<sup>45</sup> matrices that are the generators of the SU(3) group, and dictate the rotation of the quarks color in SU(3)  
<sup>46</sup> space when it interacts with a gluon. The coupling constant is encoded within  $g_s$ , which is defined by  
<sup>47</sup>  $g_s \equiv \sqrt{4\pi\alpha_s}$ . The field tensor  $F_{\mu\nu}^A$  can be written in terms of the structure constants of the SU(3) group  
<sup>48</sup>  $f_{ABC}$ , and is given by:

$$F_{\mu\nu}^A = \partial_\mu \mathcal{A}_\nu^A - \partial_\nu \mathcal{A}_\mu^A - g_s f_{ABC} \mathcal{A}^B \mathcal{A}^C \quad (1.2)$$

<sup>49</sup> While many parallels can be drawn between Quantum Electrodynamics (QED, the theory that describes  
<sup>50</sup> photons and electrons) and QCD, the difference between the two comes from the gluon-gluon interactions  
<sup>51</sup> allowed in QCD, making it non-Abelian. These interactions can be summarized as shown in Figure 1.2.

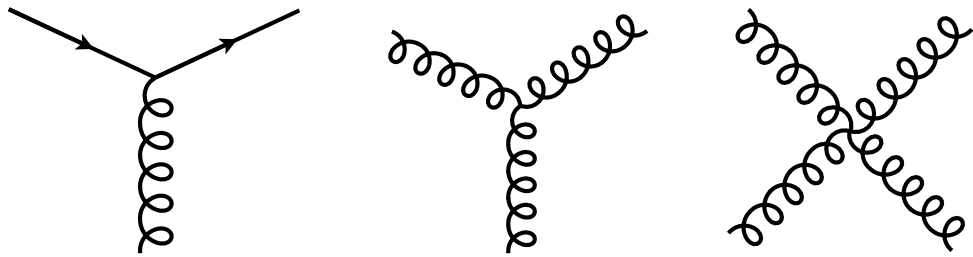


Figure 1.2: The allowed vertices in QCD. The vertices involving two or more gluons are unique to QCD and do not have a QED analog.

<sup>52</sup> A core feature of QCD is that the coupling constant  $\alpha_s$  has an energy dependence shown in Figure 1.3.  
<sup>53</sup> This dependence can be expressed in terms of the  $\beta$  function as

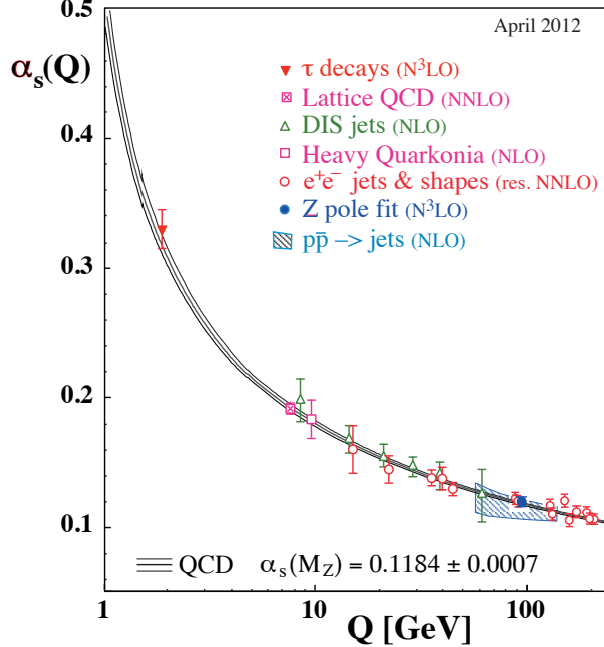


Figure 1.3: The running coupling constant  $\alpha_s$  as a function of the momentum transfer  $Q$ . Figure taken from Ref. [2].

$$Q^2 \frac{\partial \alpha_s(Q^2)}{\partial Q^2} = \beta(\alpha_s(Q^2)) \quad (1.3)$$

54 where  $Q$  is the momentum transfer in the particle reaction. The beta function can be expressed using  
 55 perturbative QCD (pQCD) as

$$\beta(\alpha_s) = -(b_0 \alpha_s^2 + b_1 \alpha_s^3 + b_2 \alpha_s^4 \dots) \quad (1.4)$$

56 where the coefficients  $b_i$  depend on the number of colors and flavors.

57 This running coupling constant is small and asymptotically tends to zero at large energy scales (or at  
 58 small distances) and is large at small energy scales (large distances). This running coupling phenomenon  
 59 leads to two key behaviors: asymptotic freedom and color confinement.

60 **Asymptotic Freedom:** At high energy scales (small distances), the QCD coupling constant  $\alpha_s$  is  
 61 small and tends to zero, implying a free particle behavior of quarks and gluons. This has been observed by a

62 variety of deep inelastic experiments [3–16]

63     **Color Confinement** The opposite end of the running coupling constant phenomenon is color confinement.  
64 This property of QCD forbids the direct observation of free quarks and gluons, allowing only for  
65 composite particles that are color singlets.

## 66     1.2 Heavy Ion Collisions and the Quark Gluon Plasma

67 Heavy ion collisions can be used as a tool to study the Quark Gluon Plasma [17] . They provide access to  
68 the otherwise confined partons, and give insight into the QCD phase diagram and the transition between the  
69 QGP and hadronic matter. This section will briefly discuss a heavy ion collision and the properties of the  
70 medium that is formed in such a collision.

### 71     1.2.1 Heavy Ion Collisions

72 In a heavy ion collision, the colliding nuclei are accelerated to relativistic energies and are Lorentz contracted  
73 discs. In the case of a Pb+Pb collision the relativistic  $\gamma$  factor is between 100 and 2500 for beam rapidities  
74 of  $y = 5.3$  and  $8.5$ . Each nucleus contains many colored quarks and antiquarks, with three more quarks than  
75 anti-quarks per nucleon, with the  $q\bar{q}$  popping in and out of the vacuum due to quantum fluctuations. These  
76  $q\bar{q}$  pairs are sources of transverse color fields and the corresponding force carriers, the gluons.

77 When these pancake like discs collide, their color fields interact and there is a color charge exchange,  
78 producing longitudinal color fields that fill the space between the receding discs. While the maximum energy  
79 density in the process occurs just at the collision, the energy density 1 fm/c after the collision is  $12 \text{ GeV/fm}^3$ ,  
80 much higher than the  $500 \text{ MeV/fm}^3$  in a typical hadron. Lattice QCD calculations in thermodynamics show  
81 that at these energies, the partons produced in the collision cannot be treated as a collection of distinct  
82 hadrons.

83 After the collision the energy density between the receding nuclei starts to decrease as the QGP cools and  
84 expands. This process, seen in Figure 1.4, continues till the energy density drops to below that within a  
85 hadron and the fluid “hadronizes”. These individual hadrons briefly scatter off of each other before they  
86 freely fly towards the detector (freeze-out).

87 While Figure 1.4 shows snapshots of a head on (central) collision between two large nuclei, it is possible to  
88 have collisions where the impact parameter is larger and hence the overlap region is smaller. These collisions,  
89 called peripheral collisions, qualitatively undergo the same process described above, with the size and shape  
90 of the QGP being different.

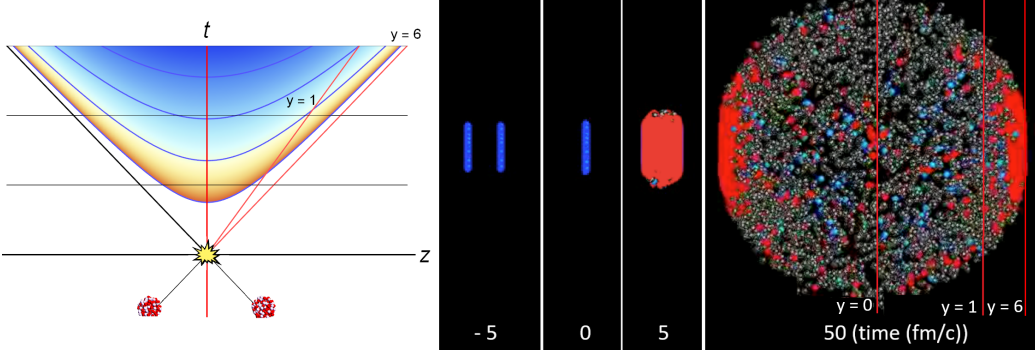


Figure 1.4: (left) Space-time diagram for a heavy ion collision. The color is indicative of the temperature of the QGP formed. (right) Snapshots of a heavy ion collision at  $\sqrt{s_{NN}} = 2.76$  TeV at different times. The Lorentz contracted nuclei are in blue while the QGP is in red. Figure from Reference [18].

91     The basic parameters of a heavy ion collision such as the number of participants  $N_{\text{part}}$  and number of  
92     binary collisions  $N_{\text{coll}}$  can be determined using the Glauber Monte Carlo simulations [19, 20]. This technique  
93     considers a nucleus-nucleus collision as a collection of independent binary nucleon-nucleon collisions; the  
94     colliding nuclei are modeled as a set of uncorrelated nucleons being positioned within the nucleus based on a  
95     the nuclear density function uniform in azimuthal and in polar angles. The nuclear density function shown in  
96     Figure 1.5 for Au and Cu, is given by:

$$\rho(r) = \rho_0 \frac{1 + w(r/R)^2}{1 + e^{\frac{r-R}{a}}} \quad (1.5)$$

97     where  $\rho_0$  is the nucleon density,  $R$  is the nuclear radius,  $a$  is the skin depth,  $w$  corresponds to deviations  
98     from a circular shape and is typically zero for larger nuclei like Cu, W, Au, Pb, and U. For the Pb nuclei  
99     used at the LHC,  $w = 0$ ,  $R = 6.62$  fm and  $a = 0.55$  fm [21].

100     They are then arranged with a random impact parameter  $b$  based on the distribution  $d\sigma/db = 2\pi b$  and  
101     projected onto the  $x - y$  plane as shown in Figure 1.6. They are then made to travel on straight trajectories,  
102     colliding if  $d \leq \sqrt{\sigma_{\text{inel}}^{\text{NN}}/\pi}$ , where  $d$  is the distance between the nucleons in a plane transverse to the beam  
103     axis and  $\sigma_{\text{inel}}^{\text{NN}}$  is the inelastic scattering cross section. [22, 23]

104     An important parameter for colliding nuclei  $A$  and  $B$  with  $A$  and  $B$  nucleons is the thickness function  
105      $T_{AB}$ . It describes the effective overlap area in which specific nucleons in the two colliding nuclei can interact.  
106     It can be defined in terms of the probability per unit area of a given nucleon being located at a particular  
107     distance  $s$  within the nucleus. For the colliding nuclei  $A$  and  $B$ , this is given by  $T_A(\mathbf{s}) = \int \rho_A(\mathbf{s}, z_A) dz_A$  and  
108      $T_B(\mathbf{s}) = \int \rho_B(\mathbf{s}, z_B) dz_B$ . Then,  $T_{AB}$  is given by

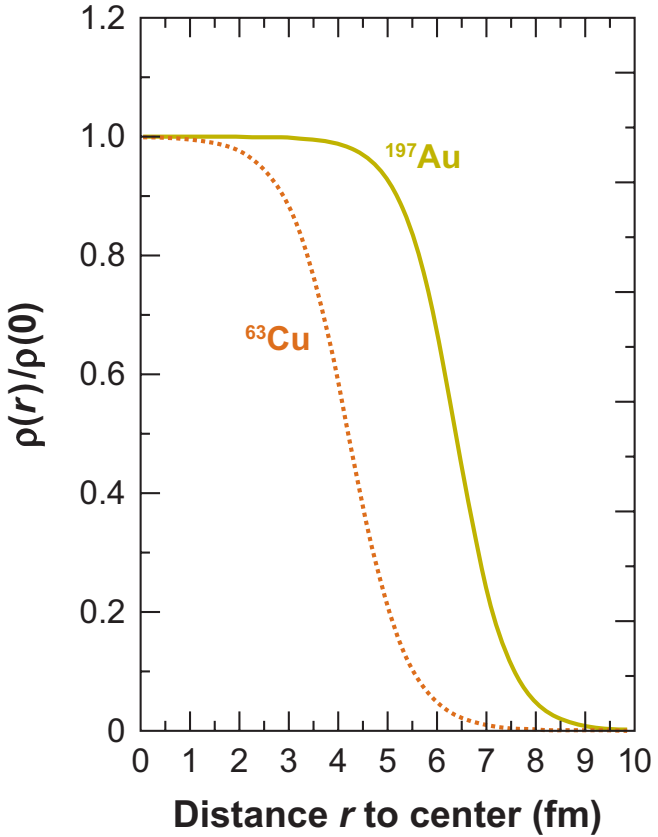


Figure 1.5: The nuclear density distributions for nuclei used at RHIC: Cu ( $w = 0$ ,  $R = 4.2$  fm and  $a = 0.48$  fm) and Au ( $w = 0$ ,  $R = 6.38$  fm and  $a = 0.535$  fm) [21, 22].

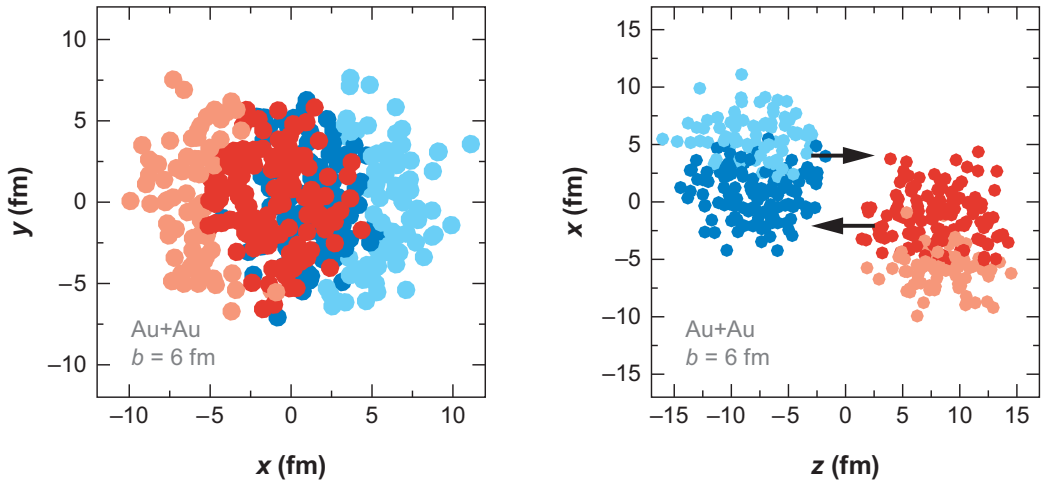


Figure 1.6: A Glauber Monte Carlo event for  $Au + Au$  at  $\sqrt{s_{NN}} = 200$  GeV with impact parameter of 6 fm viewed in the (left) transverse plane and (right) along the beam axis. Darker circles represent the participating nucleons. Taken from [22].

$$T_{AB}(\mathbf{b}) = \int T_A(\mathbf{s})T_B(\mathbf{s} - \mathbf{b})d^2s \quad (1.6)$$

109 The probability of then having  $n$  interactions between nuclei  $A$  and  $B$  is given by the binomial distribution:

$$P(n, \mathbf{b}) = \binom{AB}{n} \left[ T_{AB}(\mathbf{b})\sigma_{\text{inel}}^{\text{NN}} \right]^n \left[ 1 - T_{AB}(\mathbf{b})\sigma_{\text{inel}}^{\text{NN}} \right]^{AB-n} \quad (1.7)$$

110 where the first term is the number of combinations for finding  $n$  collisions from  $AB$  possibilities, the  
111 second term is the probability for having exactly  $n$  collisions, and the last term the probability of  $AB - n$   
112 misses. Then the total probability of an interaction between A and B is

$$\frac{d^2\sigma_{\text{inel}}^{\text{AB}}}{db^2} \equiv p_{\text{inel}}^{\text{AB}}(b) = \sum_{n=1}^{AB} P(n, \mathbf{b}) = 1 - \left[ 1 - T_{AB}(\mathbf{b})\sigma_{\text{inel}}^{\text{NN}} \right]^{AB} \quad (1.8)$$

113 Then the total cross section is given by

$$\sigma_{\text{inel}}^{\text{AB}} = \int_0^\infty 2\pi b db \left[ 1 - \left( 1 - T_{AB}(\mathbf{b})\sigma_{\text{inel}}^{\text{NN}} \right)^{AB} \right] \quad (1.9)$$

114 and  $N_{\text{coll}}$  and  $N_{\text{part}}$  are given by [24, 25]

$$N_{\text{coll}}(b) = \sum_{n=1}^{AB} n P(n, b) = AB \times T_{AB}(b)\sigma_{\text{inel}}^{\text{NN}} \quad (1.10)$$

$$N_{\text{part}}(b) = A \int T_A(\mathbf{s}) \left[ 1 - \left( 1 - T_B(\mathbf{s} - \mathbf{b})\sigma_{\text{inel}}^{\text{NN}} \right)^B \right] d^2s + B \int T_B(\mathbf{s} - \mathbf{b}) \left[ 1 - \left( 1 - T_A(\mathbf{s})\sigma_{\text{inel}}^{\text{NN}} \right)^A \right] d^2s \quad (1.11)$$

115 The correlation between  $N_{\text{coll}}$  and  $N_{\text{part}}$  can be seen in Figure 1.7

116 The charged particle multiplicity  $N_{\text{ch}}$  along with the combination of  $N_{\text{part}}$  and impact parameter  $b$  can  
117 be used to determine the centrality of a heavy ion event. An example of this is shown in Figure 1.8.

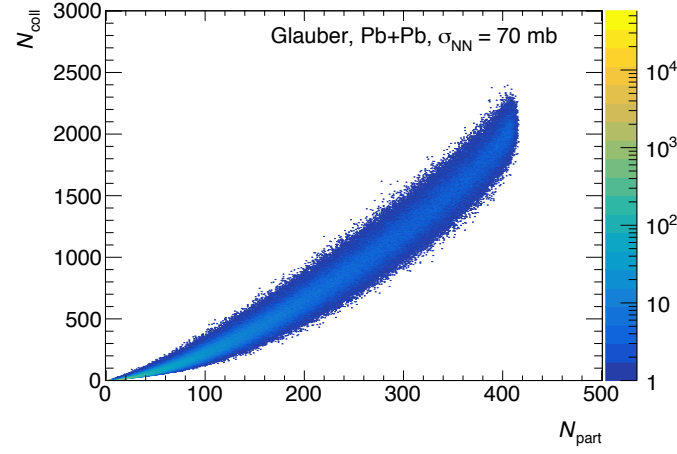


Figure 1.7: The  $N_{\text{coll}} - N_{\text{part}}$  correlation for Pb+Pb collisions at  $\sqrt{s_{\text{NN}}} = 5.02 \text{ TeV}$ . Taken from [26].

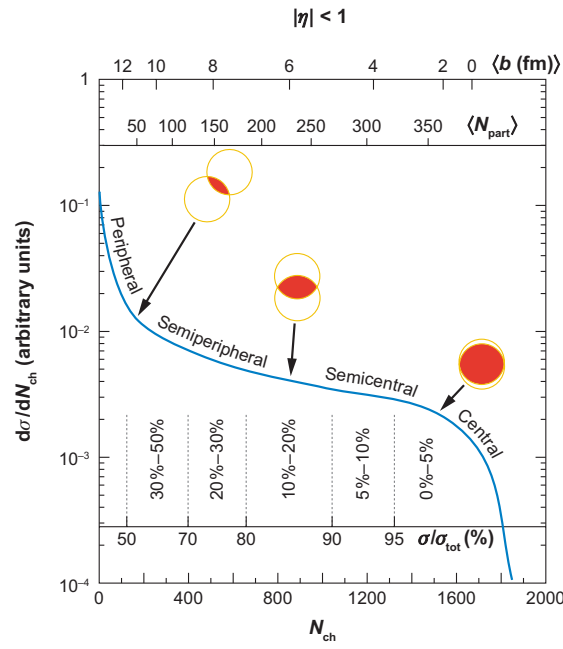


Figure 1.8: The correlation between the observable  $N_{\text{ch}}$  and  $N_{\text{part}}$  to determine the centrality distribution. Taken from [22].

### 1.2.2 The Quark Gluon Plasma

Extreme conditions of temperature and pressure like those in relativistic heavy ion collisions lead to the formation of the Quark Gluon Plasma [17]. It is believed to have filled the early universe a few microseconds after the Big Bang and might be present in the cores of extremely compact objects like neutron stars [27, 28]. The phase transition between the free quarks and gluons within the QGP and the confined quarks and gluons within hadrons can be seen in Figure 1.9.

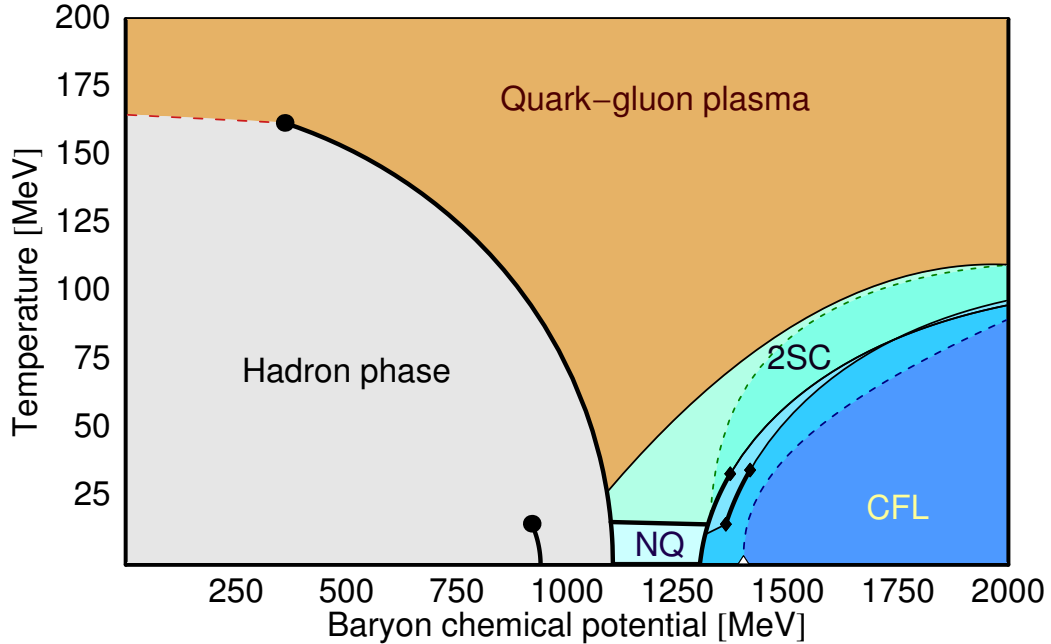


Figure 1.9: The QCD phase diagram of nuclear matter. Figure from Reference [29].

This state of matter exists for 1-10 fm/c, depending on the collision energy, above  $\lambda_{\text{QCD}} = 200$  MeV, the fundamental energy scale in QCD. Thermal photons from the QGP reveal that it reaches temperatures of 300–600 MeV in central collisions at 200 GeV [30] and 2.76 TeV [31], showing very little collision energy dependence. Further, the chemical freeze-out temperature was found to be 160 MeV via measurements of ratios of final state hadrons containing the light  $u, d$  quarks [32–34] with the thermal freeze-out being 100–150 MeV [35–38]. These measurements paint a picture of the QGP being formed early in the heavy ion collision. It has a non-uniform energy density and temperature determined by the 'colliding nuclei and collision energy. The QGP then cools and expands as described by relativistic hydrodynamics, and as its temperature falls below 160 MeV, it experiences a crossover phase transition and hadronizes. This system continues to cool and expand, until at 95 GeV there is a thermal freeze-out.

The QGP was initially thought to be a weakly coupled parton gas because of asymptotic freedom from

135 QCD. The highly energetic collisions such as those at the LHC would imply a weak interaction between the  
 136 quarks and gluons that make up the plasma. This would result in rare scatterings between the constituents  
 137 of the gas and wash out any spatial anisotropies based on the collision geometry. On the other hand, a  
 138 strong coupling within the QGP would result in the pressure gradients in the medium being driven by  
 139 hydrodynamics and spatial anisotropies would be transformed to momentum anisotropies in the particles  
 140 produced as shown in Figure 1.10. In this picture, the non-uniform structure of the colliding nuclei would  
 141 cause a momentum anisotropy that would be further enhanced when looking at collisions that are less central  
 142 and do not have perfect overlap between the colliding nuclei. These observations were seen in azimuthal  
 143 correlation measurements implying that the medium is indeed strongly coupled [39–42].

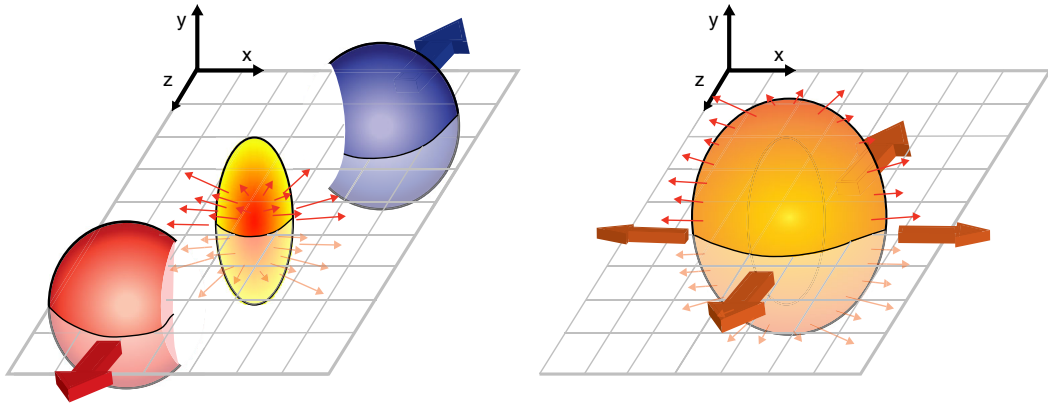


Figure 1.10: Schematic diagrams of the initial overlap region (left) and the final spatial anisotropy generated (right). Taken from [43].

144 A Fourier Transform of the angular distribution of charged hadrons in the collision debris can quantify  
 145 these momentum anisotropies and give the anisotropic flow coefficients  $v_n$ , defined as [44]:

$$\frac{d\bar{N}}{d\phi} = \frac{\bar{N}}{2\pi} \left( 1 + 2 \sum_{n=1}^{\infty} v_n \cos(n(\phi - \bar{\Psi}_n)) \right) \quad (1.12)$$

146 where  $\phi$  is the angle in the transverse plane,  $\bar{\Psi}_n$  are the event plane angles, and  $\bar{N}$  is the average number  
 147 of particles per event. Some of these coefficients are shown in Figure 1.11. The measured anisotropies can be  
 148 used to constrain the specific viscosity given by the ratio of viscosity to entropy density,  $\eta/s$ , and have shown  
 149 that the QGP has a  $\eta/s$  of near the theoretical minimum of  $1/4\pi$  [45].

150 The Bjorken energy density of the QGP can be derived using [48]:

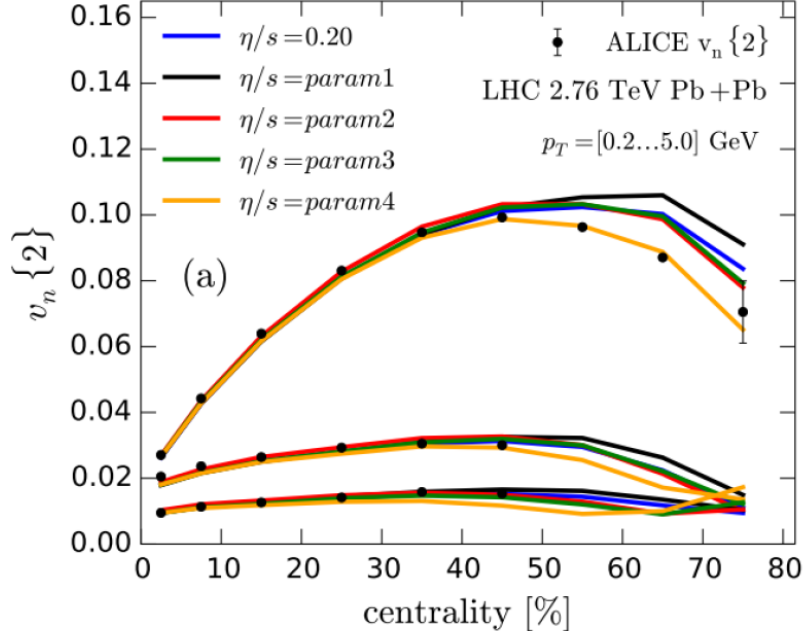


Figure 1.11: Comparison of a hydrodynamic model from [46] to anisotropy measurements by ALICE [47] for different parameterizations of  $\eta/s$  and for different  $v_n$ ,  $n = 2, 3, 4$  from top to bottom, as a function of collision centrality.

$$\varepsilon \geq \frac{dE_T/d\eta}{\tau_0 \pi R^2} = \frac{3}{2} \langle E_T/N \rangle \frac{dN_{ch}/d\eta}{\tau_0 \pi R^2} \quad (1.13)$$

where  $dN_{ch}/d\eta$  is the number of charged particles produced per unity pseudorapidity,  $dE_T/d\eta$  is the transverse energy per unit pseudorapidity,  $\tau_0$  is the thermalization time,  $R$  is the nuclear radius, and  $E_T/N \approx 1$  GeV is the transverse energy per emitted particle. As shown in Figure 1.12, the energy density at the LHC was measured to be approximately  $15$  GeV/fm $^3$ , much higher than the values measured at RHIC [49, 50].

### 1.3 Jets and Jet Quenching

Hard scatterings in particle collisions result in the production of highly energetic partons that form conical sprays of hadrons called jets. A schematic of this process is shown in Figure 1.13. Jet production in a vacuum is well described in context of perturbative QCD [52] where processes involving large momentum transfers like high  $p_T$  hadron production can be described in terms of the parton distribution functions, scattering cross sections, and final state fragmentation functions as shown below [53]:

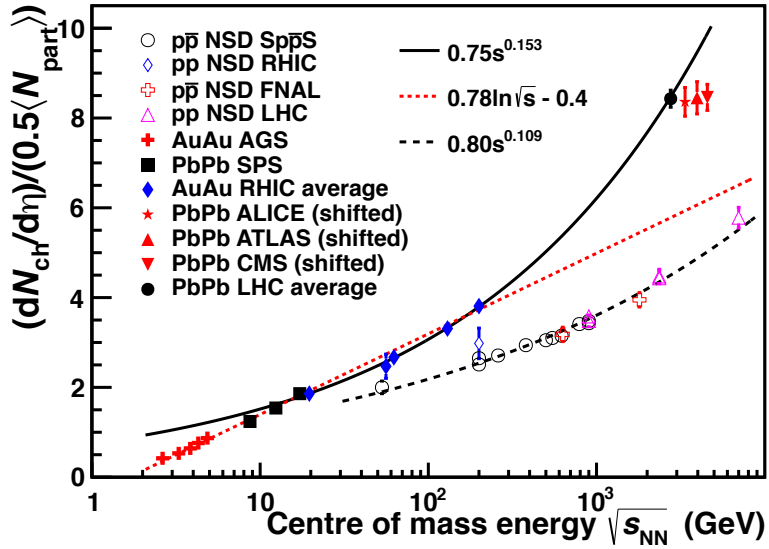


Figure 1.12:  $dN_{\text{ch}}/d\eta$  per colliding nucleon pair as a function of collision energy in  $pp$  and nucleus-nucleus collisions [51].

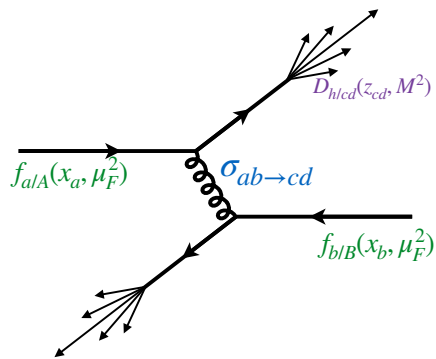


Figure 1.13: Jet production from the process  $pp \rightarrow hX$ , factorizing in terms of the parton distribution functions, scattering cross sections, and jet fragmentation functions. [53]

$$\begin{aligned}
d\sigma_{pp \rightarrow hX} &\approx \sum_{abjd} \int dx_a \int dx_b \int dz_j f_{a/p}(x_a, \mu_f) \otimes f_{b/p}(x_b, \mu_f) \\
&\otimes d\sigma_{ab \rightarrow jd}(\mu_f, \mu_F, \mu_R) \\
&\otimes D_{j \rightarrow h}(z_j, \mu_f)
\end{aligned} \tag{1.14}$$

where  $x_a = p_a/P_A, x_b = p_b/P_b$  are the initial momentum fractions carried by the interacting partons,  $z_j = p_h/p_j$  is the momentum fraction carried by the final observed hadron.  $f_{a/p}(x_a, \mu_f)$  and  $f_{b/p}(x_b, \mu_f)$  are the two parton distribution functions (PDFs),  $d\sigma_{ab \rightarrow jd}(\mu_f, \mu_F, \mu_R)$  is the differential cross section for parton scattering and  $D_{j \rightarrow h}(z_j, \mu_f)$  is the fragmentation function (FFs) for parton  $j$  to hadron  $h$ .  $\mu_f$  and  $\mu_F$  are the factorization scales and  $\mu_R$  is the renormalization scale, and are typically taken to be the same hard scale  $Q$ . The PDFs characterize the initial state and represent the probability of finding a parton with momentum fraction  $x$  (shown in Figure 1.14) in the initial hadron, while the FFs describe the probability of fragmenting to a hadron  $h$  with given kinematic properties.

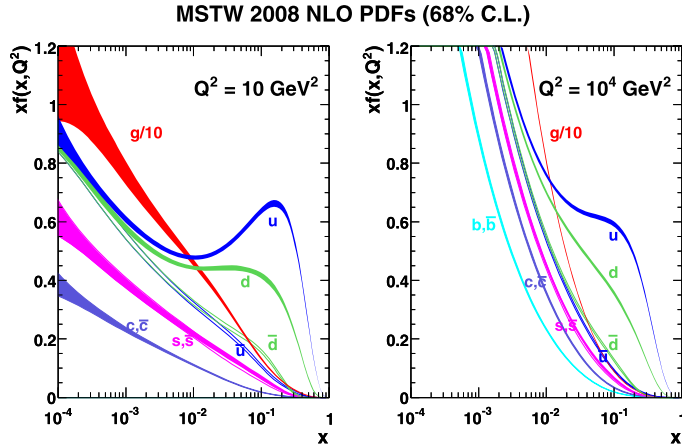


Figure 1.14: The next to leading order (NLO) PDFs at (left)  $Q^2 = 10 \text{ GeV}^2$  and (right)  $Q^2 = 10^4 \text{ GeV}^2$ . The band is the associated one-sigma (68%) confidence level uncertainty. Taken from [54]

In the case of heavy ion collisions, the jet observables can be modified due to two sources: the nuclear PDF being distinct from a proton PDF, and the formation of the quark gluon plasma. The former is collectively referred to as cold nuclear matter (CNM) effect, and can be quantified by defining a nuclear modification factor for the PDF:

$$R_a^A(x, Q^2) = \frac{f_{a/A}(x, Q^2)}{f_{a/p}(x, Q^2)} \quad (1.15)$$

where  $f_{a/A}$  and  $f_{a/p}$  are the nuclear and proton PDFs respectively. This  $R_a^A$  factor is determined by global fits to data from DIS measurements [55–57]. CNM effects include the following contributions:

- Shadowing: This is a destructive interference effect that reduces the interactions of a nucleon incident on a nucleus within its interior and on its back face. This effect reduces the effective number of nucleons in an inelastic interaction to  $A^{2/3}$ . For  $Q^2$  of the order of a few  $\text{GeV}^2$ , this effect dominates for  $x < 0.05$  and implies  $R_a^A(x, Q^2) < 1$  [58].
- Anti-shadowing: This compensates for the shadowing effect based on the momentum sum rule, and for  $Q^2$  of the order of a few  $\text{GeV}^2$  implies  $R_a^A(x, Q^2) > 1$  over the region  $0.05 < x < 0.20$ .
- EMC: The modification of the nuclear structure function was first observed by the European Muon Collaboration [59]. Recent observations have suggested that the effect is caused by short-range correlated nucleon pairs within nuclei [60]. For  $Q^2$  of the order of a few  $\text{GeV}^2$ , this effect dominates for  $0.2 < x < 0.80$  and implies  $R_a^A(x, Q^2) < 1$ .
- Fermi Motion: This effect considers the motion of the nucleons within the nucleus. It results in  $R_a^A(x, Q^2) > 1$  over the  $x > 0.8$  region for  $Q^2$  of the order of a few  $\text{GeV}^2$  [61].

Cold nuclear matter effects are experimentally measured using  $p + A$  systems where the size and shape of the plasma, and hence any effects thereof, are a lot smaller.

The second source of modification is the formation of the hot and dense quark gluon plasma. The hot nuclear matter effects further serve as an independent confirmation that the medium formed is strongly interacting. Jets are formed early enough that they traverse the Quark Gluon Plasma and as strongly interacting particles, are both affected by, and affect the QGP. This interaction typically results in the jet losing energy and forward momentum [62, 63], with the lost energy being deposited in the medium [64]. Jets can also pick up momentum transverse to the parton direction [65]. The hot nuclear matter effects can be considered to be a combination of collisional and radiative energy losses summarized in Figure 1.15.

- Collisional energy loss: This is a combination of elastic and inelastic collisions of the hard parton with the constituents of the quark gluon plasma.
- Radiative energy loss: This is the larger source of parton energy loss and jet quenching. These are modified by the presence of the plasma due to scatterings off of the plasma constituents. A variety of

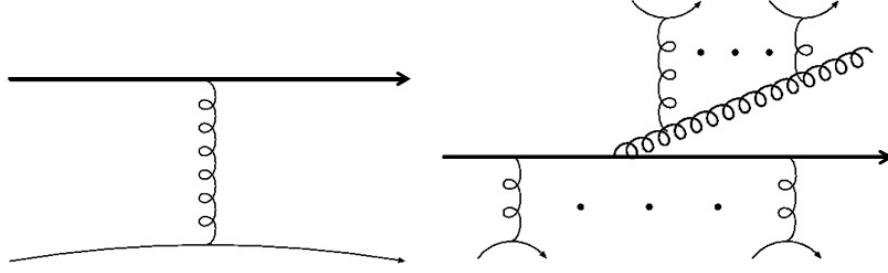


Figure 1.15: The typical diagrams for (left) collisional and (right) radiative energy losses for a parton in a hard scattering as it propagates through the QGP. Taken from [53]

radiative energy loss frameworks that have been developed include: Baier-Dokshitzer-Mueller-Peigne-Schiff-Zakharov (BDMPS-Z) [66], Gyulassy, Levai and Vitev (GLV) [67], Amesto-Salgado-Wiedemann (ASW) [68], Arnold-Moore-Yaffe (AMY) [69] and higher twist (HT) [70].

**Collisional energy loss** This is a combination of elastic and inelastic collisions of the hard parton with the constituents of the quark gluon plasma. The

Both hot and cold nuclear matter effects can be described by modifying Equation 1.14 as:

$$d\sigma_{AB \rightarrow hX} \approx \sum_{abjj'd} f_{a/A}(x_a) \otimes f_{b/B}(x_b) \otimes d\sigma_{ab \rightarrow jd}(\mu_f, \mu_F, \mu_R) \otimes P_{j \rightarrow j'} \otimes D_{h \rightarrow j'}(z_j, \mu_f) \quad (1.16)$$

where the additional  $P_{j \rightarrow j'}$  describes the interaction of the hard parton with the colored medium. This is typically taken as part of the fragmentation modification as:

$$\tilde{D}_{h \rightarrow j'}(z_j, \mu_f) \approx \sum_{j'} P_{j \rightarrow j'}(p_{j'}|p_j) \otimes D_{h \rightarrow j'}(j') \quad (1.17)$$

A few jet measurements and their modifications by the presence of the Quark Gluon Plasma are discussed in Section 2.

# Chapter 2

## Major Jet Measurements

209 This chapter shall discuss some important experimental jet measurements that motivate the study of the  
210 main analysis in this thesis. It will begin with a brief discussion of the jet reconstruction procedure and go  
211 on to discuss measurements of jet yields, dijet asymmetry, and jet fragmentation.

### 212 2.1 Jet Reconstruction

213 Jets can be reconstructed by clustering algorithms that take in a variety of inputs. The algorithm used in  
214 ATLAS is the anti- $k_t$  clustering algorithm [71]. This algorithm clusters soft particles around hard ones in the  
215 following manner:

- 216 • Calculate all distances  $d_{ij}$  between entities  $i$  and  $j$ , and distance  $d_{iB}$  between entity  $i$  and beam  $B$ .
- 217 • Identify the smallest distances such that for the smallest distance  $d_{ij}$ , the entities  $i$  and  $j$  are combined  
218 and return to beginning.
- 219 • If the smallest distance is  $d_{iB}$ , then take  $i$  as the jet and remove it from the list of entities and return  
220 to beginning.
- 221 • Continue the procedure till the list of items is empty.

222 In general the distance  $d_{ij}$  between the objects is found via the prescription

$$d_{ij} = \min(k_{Ti}^{2p}, k_{Tj}^{2p}) \frac{\Delta_{ij}^2}{R^2} \quad (2.1)$$

$$d_{iB} = k_{Ti}^{2p} \quad (2.2)$$

223 where  $k_{Ti}$  is the transverse momentum of particle  $i$  and  $\Delta_{ij} = \sqrt{\Delta\eta_{ij}^2 + \Delta\phi_{ij}^2}$  is the distance between  
224 particles  $i$  and  $j$  in  $\eta - \phi$  space.  $R$  the distance parameter and reflects the size of the jet being considered. In the

case of the anti- $k_t$  algorithm,  $p = -1$ . Other popular clustering algorithms like  $k_t$  [72] and Cambridge/Aachen [73] use  $p = 1$  and  $p = 0$  respectively. The behavior of the different clustering algorithms is shown in Figure 2.1.

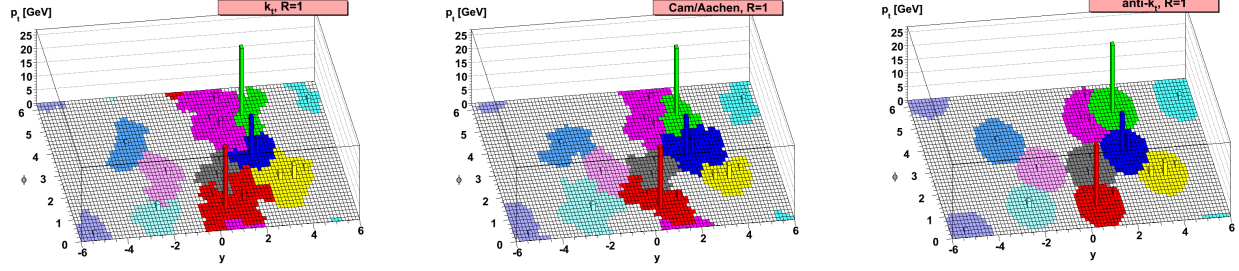


Figure 2.1: Different clustering algorithms applied to the sample parton-level event. Figure taken from [71].

The popularity of the anti- $k_t$  algorithm comes from its overcoming of two common problems: collinear and infrared safety. These are related to instabilities in the cones that are found due to soft radiation.

Figure 2.2 describes the collinear safety problem. In a collinear safe jet algorithm, the presence of a virtual loop or a collinear splitting of a central particle would not change the number of jets being reconstructed. On the other hand, while a collinear unsafe jet algorithm would not change its output with the presence of a virtual loop, a splitting in the central particle would lead to the left and right most particles forming individual seeds, implying two reconstructed jets [74].

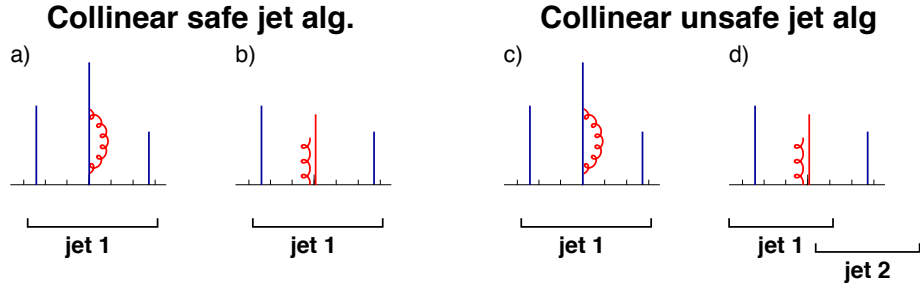


Figure 2.2: An illustration of collinear unsafe behavior. The particle  $p_T$  is proportional to the height and the horizontal axis indicates rapidity. Taken from [74].

A schematic describing infrared un-safety is shown in Figure 2.3. Here an infrared safe algorithm would use the three particles as seeds iteratively find two stable cones. An unsafe algorithm however would find three overlapping cones based on the addition of a soft seed.

For heavy ion collisions in ATLAS, the inputs to the algorithm are the  $\eta \times \phi = 0.1 \times 0.1$  calorimeter towers. The tower energies are determined by summing up the energies of the individual calorimeter cells. The anti- $k_t$  algorithm is first run with the distance parameter  $R = 0.2$ , following which an underlying event

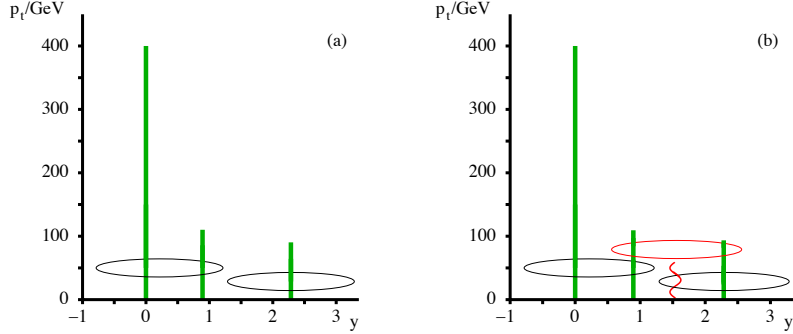


Figure 2.3: An illustration of infrared unsafe behavior. The particle  $p_T$  is proportional to the height and the horizontal axis indicates rapidity. Taken from [75]

241 subtraction procedure is performed. A first estimate of the average underlying event energy density  $\rho_i(\eta)$  is  
 242 done in 0.1 slices of  $\eta$  in each calorimeter layer  $i$  after excluding the regions that overlap with the seed jets.  
 243 A modulation of  $2v_2 \cos[2(\phi - \Psi_2)]$  is applied to account for the flow from the QGP and the underlying event  
 244 is subtracted to give  $E_{Tj}^{\text{sub}}$ :

$$E_{Tj}^{\text{sub}} = E_{Tj} - A_j \rho_i(\eta_j) 1 + 2v_{2i} (\cos[2(\phi - \Psi_2)]) \quad (2.3)$$

245 where  $E_{Tj}$ ,  $\eta_j$ ,  $\phi_j$  and  $A_j$  are the cell  $E_T$ ,  $\eta$ ,  $\phi$  and area for cell  $j$  in layer  $i$ . This process is done iteratively  
 246 done one more time after getting new seeds with the distance parameter  $R = 0.2$  and excluding areas that  
 247 are within  $\Delta R = 0.4$  of the seeds. Updated values of  $\rho'_i$  and  $v'_2$  are recalculated and used to estimate the  
 248 background that is subtracted from the original cell energies. More details on this procedure can be found in  
 249 [76]

## 250 2.2 Modification of jet yields: Jet $R_{AA}$

251 Jet  $R_{AA}$  and Jet  $R_{AA}$

## 252 2.3 Jet $X_J$

## 253 2.4 Jet Fragmentation

# Bibliography

- 254 [1] M. K. Gaillard, P. D. Grannis and F. J. Sciulli, *The Standard model of particle physics*, Rev. Mod.  
255 Phys. **71** (1999) S96, arXiv: [hep-ph/9812285 \[hep-ph\]](#) (cit. on p. 1).
- 256 [2] J Beringer et al., *Review of Particle Physics, 2012-2013. Review of Particle Properties*, Phys. Rev. D  
257 **86** (2012) 010001 (cit. on pp. 2, 3).
- 258 [3] A. Deur et al., *High precision determination of the  $Q^2$  evolution of the Bjorken Sum*, Phys. Rev. D**90**  
259 (2014) 012009, arXiv: [1405.7854 \[nucl-ex\]](#) (cit. on p. 4).
- 260 [4] J. H. Kim et al., *A Measurement of  $\alpha_s(Q^2)$  from the Gross-Llewellyn Smith sum rule*, Phys. Rev. Lett.  
261 **81** (1998) 3595, arXiv: [hep-ex/9808015 \[hep-ex\]](#) (cit. on p. 4).
- 262 [5] G. Altarelli et al., *Determination of the Bjorken sum and strong coupling from polarized structure  
263 functions*, Nucl. Phys. **B496** (1997) 337, arXiv: [hep-ph/9701289 \[hep-ph\]](#) (cit. on p. 4).
- 264 [6] H. W. Kendall, *Deep inelastic scattering: Experiments on the proton and the observation of scaling*,  
265 Rev. Mod. Phys. **63** (3 1991) 597 (cit. on p. 4).
- 266 [7] A. L. Kataev, G. Parente and A. V. Sidorov, *Improved fits to the  $xF_3$  CCFR data at the next-to-next-to-  
267 leading order and beyond*, Phys. Part. Nucl. **34** (2003) 20, [Erratum: Phys. Part. Nucl.38,no.6,827(2007)],  
268 arXiv: [hep-ph/0106221 \[hep-ph\]](#) (cit. on p. 4).
- 269 [8] S. Alekhin, J. Blumlein and S. Moch, *Parton Distribution Functions and Benchmark Cross Sections at  
270 NNLO*, Phys. Rev. D**86** (2012) 054009, arXiv: [1202.2281 \[hep-ph\]](#) (cit. on p. 4).
- 271 [9] S. Alekhin, J. Blumlein and S.-O. Moch, *ABM news and benchmarks*, PoS **DIS2013** (2013) 039, arXiv:  
272 [1308.5166 \[hep-ph\]](#) (cit. on p. 4).
- 273 [10] J. Blumlein, H. Bottcher and A. Guffanti, *Non-singlet QCD analysis of deep inelastic world data at  
274  $O(\alpha_s^3)$* , Nucl. Phys. **B774** (2007) 182, arXiv: [hep-ph/0607200 \[hep-ph\]](#) (cit. on p. 4).
- 275 [11] H1 Collaboration, *Three- and Four-jet Production at Low  $x$  at HERA*, Eur. Phys. J. C**54** (2008) 389,  
276 arXiv: [0711.2606 \[hep-ex\]](#) (cit. on p. 4).

- 277 [12] ZEUS Collaboration, *Forward-jet production in deep inelastic ep scattering at HERA*, *Eur. Phys. J.*  
 278 **C52** (2007) 515, arXiv: [0707.3093 \[hep-ex\]](#) (cit. on p. 4).
- 279 [13] ZEUS Collaboration, *Multi-jet cross-sections in charged current  $e^\pm p$  scattering at HERA*, *Phys. Rev.*  
 280 **D78** (2008) 032004, arXiv: [0802.3955 \[hep-ex\]](#) (cit. on p. 4).
- 281 [14] ZEUS Collaboration, *Inclusive dijet cross sections in neutral current deep inelastic scattering at HERA*,  
 282 *Eur. Phys. J. C70* (2010) 965, arXiv: [1010.6167 \[hep-ex\]](#) (cit. on p. 4).
- 283 [15] ZEUS Collaboration, *Inclusive-jet cross sections in NC DIS at HERA and a comparison of the  $kT$ ,*  
 284 *anti- $kT$  and SIScone jet algorithms*, *Phys. Lett. B691* (2010) 127, arXiv: [1003.2923 \[hep-ex\]](#) (cit. on  
 285 p. 4).
- 286 [16] H1 Collaboration, *Jet Production in ep Collisions at High  $Q^2$  and Determination of  $\alpha_s$* , *Eur. Phys. J.*  
 287 **C65** (2010) 363, arXiv: [0904.3870 \[hep-ex\]](#) (cit. on p. 4).
- 288 [17] E. V. Shuryak, *Quantum chromodynamics and the theory of superdense matter*, *Physics Reports*  
 289 **61** (1980) 71 , ISSN: 0370-1573, URL: <http://www.sciencedirect.com/science/article/pii/0370157380901052> (cit. on pp. 4, 9).
- 291 [18] W. Busza et al., *Heavy Ion Collisions: The Big Picture, and the Big Questions*, *Ann. Rev. Nucl. Part.*  
 292 *Sci. 68* (2018) 339, arXiv: [1802.04801 \[hep-ph\]](#) (cit. on p. 5).
- 293 [19] R. Glauber, *Lectures in theoretical physics*, ed. WE Brittin and LG Dunham, Interscience, New York **1**  
 294 (1959) 315 (cit. on p. 5).
- 295 [20] R. Glauber et al., *Lectures in theoretical physics*, 1959 (cit. on p. 5).
- 296 [21] H. D. Vries, C. D. Jager and C. D. Vries, *Nuclear charge-density-distribution parameters from elastic*  
 297 *electron scattering*, *Atomic Data and Nuclear Data Tables* **36** (1987) 495 , ISSN: 0092-640X, URL:  
 298 <http://www.sciencedirect.com/science/article/pii/0092640X87900131> (cit. on pp. 5, 6).
- 299 [22] M. L. Miller, K. Reygers, S. J. Sanders and P. Steinberg, *Glauber Modeling in High-Energy Nuclear*  
 300 *Collisions*, *Annual Review of Nuclear and Particle Science* **57** (2007) 205, eprint: <https://doi.org/10.1146/annurev.nucl.57.090506.123020>, URL: <https://doi.org/10.1146/annurev.nucl.57.090506.123020> (cit. on pp. 5, 6, 8).
- 303 [23] B. Alver, M. Baker, C. Loizides and P. Steinberg, *The PHOBOS Glauber Monte Carlo*, (2008), arXiv:  
 304 [0805.4411 \[nucl-ex\]](#) (cit. on p. 5).
- 305 [24] D. Kharzeev and M. Nardi, *Hadron production in nuclear collisions at RHIC and high density QCD*,  
 306 *Phys. Lett. B507* (2001) 121, arXiv: [nucl-th/0012025 \[nucl-th\]](#) (cit. on p. 7).

- 307 [25] A. Bialas, M. Bleszynski and W. Czyz, *Multiplicity Distributions in Nucleus-Nucleus Collisions at*  
 308 *High-Energies*, Nucl. Phys. **B111** (1976) 461 (cit. on p. 7).
- 309 [26] ATLAS Collaboration, *Centrality determination in  $\sqrt{s_{NN}} = 5.02 \text{ TeV Pb+Pb collision data in 2015}$* ,  
 310 tech. rep. ATL-COM-PHYS-2016-1287, CERN, 2016, URL: <https://cds.cern.ch/record/2212936>  
 311 (cit. on p. 8).
- 312 [27] J. C. Collins and M. J. Perry, *Superdense Matter: Neutrons or Asymptotically Free Quarks?*, Phys. Rev.  
 313 Lett. **34** (21 1975) 1353, URL: <https://link.aps.org/doi/10.1103/PhysRevLett.34.1353> (cit. on  
 314 p. 9).
- 315 [28] A. D. Linde, *Phase transitions in gauge theories and cosmology*, Reports on Progress in Physics **42**  
 316 (1979) 389, URL: <https://doi.org/10.1088%2F0034-4885%2F42%2F3%2F001> (cit. on p. 9).
- 317 [29] S. B. Ruster, V. Werth, M. Buballa, I. A. Shovkovy and D. H. Rischke, *Phase diagram of neutral*  
 318 *quark matter: Self-consistent treatment of quark masses*, Phys. Rev. D **72** (3 2005) 034004, URL:  
 319 <https://link.aps.org/doi/10.1103/PhysRevD.72.034004> (cit. on p. 9).
- 320 [30] PHENIX Collaboration, *Enhanced Production of Direct Photons in Au + Au Collisions at  $\sqrt{s_{NN}} =$*   
 321 *200 GeV and Implications for the Initial Temperature*, Phys. Rev. Lett. **104** (13 2010) 132301, URL:  
 322 <https://link.aps.org/doi/10.1103/PhysRevLett.104.132301> (cit. on p. 9).
- 323 [31] ALICE Collaboration, *Direct photon production in Pb–Pb collisions at  $s_{NN}=2.76 \text{ TeV}$* , Physics Letters  
 324 **B 754** (2016) 235 , ISSN: 0370-2693, URL: <http://www.sciencedirect.com/science/article/pii/S0370269316000320> (cit. on p. 9).
- 326 [32] Z. Fodor and S. Katz, *Critical point of QCD at finite T and  $\lambda$ , lattice results for physical quark*  
 327 *masses*, Journal of High Energy Physics **2004** (2004) 050, URL: <https://doi.org/10.1088%2F1126-6708%2F2004%2F04%2F050> (cit. on p. 9).
- 329 [33] STAR Collaboration, *Experimental and theoretical challenges in the search for the quark-gluon plasma: The STAR Collaboration's critical assessment of the evidence from RHIC collisions*, Nuclear Physics  
 330 **A 757** (2005) 102 , First Three Years of Operation of RHIC, ISSN: 0375-9474, URL: <http://www.sciencedirect.com/science/article/pii/S0375947405005294> (cit. on p. 9).
- 333 [34] ALICE Collaboration, *Production of light nuclei and anti-nuclei in pp and Pb-Pb collisions at energies*  
 334 *available at the CERN Large Hadron Collider*, Phys. Rev. C **93** (2 2016) 024917, URL: <https://link.aps.org/doi/10.1103/PhysRevC.93.024917> (cit. on p. 9).

- 336 [35] PHENIX Collaboration, *Single identified hadron spectra from  $\sqrt{s_{NN}} = 130$  GeV Au + Au collisions*,  
 337 Phys. Rev. C **69** (2 2004) 024904, URL: <https://link.aps.org/doi/10.1103/PhysRevC.69.024904>  
 338 (cit. on p. 9).
- 339 [36] BRAHMS Collaboration, *Centrality dependent particle production at  $y = 0$  and  $y \approx 1$  in Au+Au collisions*  
 340 at  $\sqrt{s_{NN}} = 200$  GeV, Phys. Rev. C **72** (1 2005) 014908, URL: <https://link.aps.org/doi/10.1103/PhysRevC.72.014908> (cit. on p. 9).
- 342 [37] PHOBOS Collaboration, *Identified hadron transverse momentum spectra in Au+Au collisions at*  
 343  $\sqrt{s_{NN}} = 62.4$  GeV, Phys. Rev. C **75** (2 2007) 024910, URL: <https://link.aps.org/doi/10.1103/PhysRevC.75.024910> (cit. on p. 9).
- 345 [38] ALICE Collaboration, *Centrality dependence of  $\pi$ ,  $K$ , and  $p$  production in Pb-Pb collisions at  $\sqrt{s_{NN}} =$*   
 346  $2.76$  TeV, Phys. Rev. C **88** (4 2013) 044910, URL: <https://link.aps.org/doi/10.1103/PhysRevC.88.044910> (cit. on p. 9).
- 348 [39] ATLAS Collaboration, *Measurement of the azimuthal anisotropy of charged particles produced in  $\sqrt{s_{NN}} =$*   
 349  $5.02$  TeV Pb+Pb collisions with the ATLAS detector, Eur. Phys. J. **C78** (2018) 997, arXiv: [1808.03951](https://arxiv.org/abs/1808.03951)  
 350 [nucl-ex] (cit. on p. 10).
- 351 [40] PHENIX Collaboration, *Elliptic Flow of Identified Hadrons in Au+Au Collisions at  $\sqrt{s_{NN}} = 200$  GeV*,  
 352 Phys. Rev. Lett. **91** (18 2003) 182301, URL: <https://link.aps.org/doi/10.1103/PhysRevLett.91.182301> (cit. on p. 10).
- 354 [41] CMS Collaboration, *Non-Gaussian elliptic-flow fluctuations in PbPb collisions at  $\sqrt{s_{NN}} = 5.02$  TeV*,  
 355 Phys. Lett. **B789** (2019) 643, arXiv: [1711.05594](https://arxiv.org/abs/1711.05594) [nucl-ex] (cit. on p. 10).
- 356 [42] ALICE Collaboration, *Anisotropic Flow of Charged Particles in Pb-Pb Collisions at  $\sqrt{s_{NN}} = 5.02$  TeV*,  
 357 Phys. Rev. Lett. **116** (13 2016) 132302, URL: <https://link.aps.org/doi/10.1103/PhysRevLett.116.132302> (cit. on p. 10).
- 359 [43] M. Connors, C. Nattrass, R. Reed and S. Salur, *Jet measurements in heavy ion physics*, Rev. Mod. Phys.  
 360 **90** (2 2018) 025005, URL: <https://link.aps.org/doi/10.1103/RevModPhys.90.025005> (cit. on  
 361 p. 10).
- 362 [44] A. M. Poskanzer and S. A. Voloshin, *Methods for analyzing anisotropic flow in relativistic nuclear*  
 363 *collisions*, Phys. Rev. **C58** (1998) 1671, arXiv: [nucl-ex/9805001](https://arxiv.org/abs/nucl-ex/9805001) [nucl-ex] (cit. on p. 10).
- 364 [45] U. Heinz and R. Snellings, *Collective flow and viscosity in relativistic heavy-ion collisions*, Ann. Rev.  
 365 Nucl. Part. Sci. **63** (2013) 123, arXiv: [1301.2826](https://arxiv.org/abs/1301.2826) [nucl-th] (cit. on p. 10).

- [46] H. Niemi, K. J. Eskola and R. Paatelainen, *Event-by-event fluctuations in a perturbative QCD + saturation + hydrodynamics model: Determining QCD matter shear viscosity in ultrarelativistic heavy-ion collisions*, Phys. Rev. **C93** (2016) 024907, arXiv: [1505.02677 \[hep-ph\]](https://arxiv.org/abs/1505.02677) (cit. on p. 11).
- [47] ALICE Collaboration, *Higher harmonic anisotropic flow measurements of charged particles in Pb-Pb collisions at  $\sqrt{s_{NN}}=2.76$  TeV*, Phys. Rev. Lett. **107** (2011) 032301, arXiv: [1105.3865 \[nucl-ex\]](https://arxiv.org/abs/1105.3865) (cit. on p. 11).
- [48] J. D. Bjorken, *Highly relativistic nucleus-nucleus collisions: The central rapidity region*, Phys. Rev. D **27** (1 1983) 140, URL: <https://link.aps.org/doi/10.1103/PhysRevD.27.140> (cit. on p. 10).
- [49] PHENIX Collaboration, *Formation of dense partonic matter in relativistic nucleus-nucleus collisions at RHIC: Experimental evaluation by the PHENIX collaboration*, Nucl. Phys. **A757** (2005) 184, arXiv: [nucl-ex/0410003 \[nucl-ex\]](https://arxiv.org/abs/nucl-ex/0410003) (cit. on p. 11).
- [50] CMS Collaboration, *Charged hadron multiplicity and transverse energy densities in PbPb collisions from CMS*, Journal of Physics G: Nuclear and Particle Physics **38** (2011) 124041, URL: <https://doi.org/10.1088%2F0954-3899%2F38%2F12%2F124041> (cit. on p. 11).
- [51] B. Muller, J. Schukraft and B. Wyslouch, *First Results from Pb+Pb collisions at the LHC*, Ann. Rev. Nucl. Part. Sci. **62** (2012) 361, arXiv: [1202.3233 \[hep-ex\]](https://arxiv.org/abs/1202.3233) (cit. on p. 12).
- [52] T. Sjostrand, S. Mrenna and P. Z. Skands, *A Brief Introduction to PYTHIA 8.1*, Comput. Phys. Commun. **178** (2008) 852, arXiv: [0710.3820 \[hep-ph\]](https://arxiv.org/abs/0710.3820) (cit. on p. 11).
- [53] G.-Y. Qin and X.-N. Wang, *Jet quenching in high-energy heavy-ion collisions*, Int. J. Mod. Phys. E **24** (2015) 1530014, arXiv: [1511.00790 \[hep-ph\]](https://arxiv.org/abs/1511.00790) [hep-ph] (cit. on pp. 11, 12, 15).
- [54] A. D. Martin, W. J. Stirling, R. S. Thorne and G. Watt, *Parton distributions for the LHC*, The European Physical Journal C **63** (2009) 189, ISSN: 1434-6052, URL: <https://doi.org/10.1140/epjc/s10052-009-1072-5> (cit. on p. 13).
- [55] M. Hirai, S. Kumano and T.-H. Nagai, *Determination of nuclear parton distribution functions and their uncertainties at next-to-leading order*, Phys. Rev. C **76** (6 2007) 065207, URL: <https://link.aps.org/doi/10.1103/PhysRevC.76.065207> (cit. on p. 14).
- [56] D. de Florian and R. Sassot, *Nuclear parton distributions at next to leading order*, Phys. Rev. D **69** (7 2004) 074028, URL: <https://link.aps.org/doi/10.1103/PhysRevD.69.074028> (cit. on p. 14).
- [57] K. Eskola, H Paukkunen and C. Salgado, *EPS09 — A new generation of NLO and LO nuclear parton distribution functions*, Journal of High Energy Physics **2009** (2009) 065, URL: <https://doi.org/10.1088%2F1126-6708%2F2009%2F04%2F065> (cit. on p. 14).

- 397 [58] S. J. Brodsky and H. J. Lu, *Shadowing and antishadowing of nuclear structure functions*, Phys. Rev.  
 398 Lett. **64** (12 1990) 1342, URL: <https://link.aps.org/doi/10.1103/PhysRevLett.64.1342> (cit. on  
 399 p. 14).
- 400 [59] European Muon Collaboration, *The ratio of the nucleon structure functions F2N for iron and deuterium*,  
 401 Physics Letters B **123** (1983) 275 , ISSN: 0370-2693, URL: <http://www.sciencedirect.com/science/article/pii/0370269383904379> (cit. on p. 14).
- 402 [60] O. Hen, E. Piasetzky and L. B. Weinstein, *New data strengthen the connection between short range*  
 403 *correlations and the EMC effect*, Phys. Rev. C **85** (4 2012) 047301, URL: <https://link.aps.org/doi/10.1103/PhysRevC.85.047301> (cit. on p. 14).
- 404 [61] K. Saito and T. Uchiyama, *Effect of the Fermi Motion on Nuclear Structure Functions and the Emc*  
 405 *Effect*, Z. Phys. **A322** (1985) 299 (cit. on p. 14).
- 406 [62] CMS Collaboration, *Jet momentum dependence of jet quenching in PbPb collisions at sNN=2.76 TeV*,  
 407 Physics Letters B **712** (2012) 176 , ISSN: 0370-2693, URL: <http://www.sciencedirect.com/science/article/pii/S037026931200487X> (cit. on p. 14).
- 408 [63] ATLAS collaboration, *Study of inclusive jet yields in Pb+Pb collisions at  $\sqrt{s_{NN}} = 5.02$  TeV*, (2017)  
 409 (cit. on p. 14).
- 410 [64] The CMS collaboration, *Measurement of transverse momentum relative to dijet systems in PbPb and*  
 411 *pp collisions at  $\sqrt{s_{NN}} = 2.76$  TeV*, Journal of High Energy Physics **2016** (2016) 6, ISSN: 1029-8479, URL:  
 412 [https://doi.org/10.1007/JHEP01\(2016\)006](https://doi.org/10.1007/JHEP01(2016)006) (cit. on p. 14).
- 413 [65] S. Chatrchyan et al., *Jet momentum dependence of jet quenching in PbPb collisions at  $\sqrt{s_{NN}} = 2.76$*   
 414 *TeV*, Phys. Lett. **B712** (2012) 176, arXiv: [1202.5022 \[nucl-ex\]](https://arxiv.org/abs/1202.5022) (cit. on p. 14).
- 415 [66] R. Baier, Y. Dokshitzer, A. Mueller, S. Peigné and D. Schiff, *Radiative energy loss of high energy quarks*  
 416 *and gluons in a finite-volume quark-gluon plasma*, Nuclear Physics B **483** (1997) 291 , ISSN: 0550-3213,  
 417 URL: <http://www.sciencedirect.com/science/article/pii/S0550321396005536> (cit. on p. 15).
- 418 [67] M. Gyulassy, P. Levai and I. Vitev, *Jet quenching in thin quark gluon plasmas. 1. Formalism*, Nucl.  
 419 Phys. **B571** (2000) 197, arXiv: [hep-ph/9907461 \[hep-ph\]](https://arxiv.org/abs/hep-ph/9907461) (cit. on p. 15).
- 420 [68] U. A. Wiedemann, *Gluon radiation off hard quarks in a nuclear environment: Opacity expansion*, Nucl.  
 421 Phys. **B588** (2000) 303, arXiv: [hep-ph/0005129 \[hep-ph\]](https://arxiv.org/abs/hep-ph/0005129) (cit. on p. 15).
- 422 [69] P. B. Arnold, G. D. Moore and L. G. Yaffe, *Photon emission from ultrarelativistic plasmas*, JHEP **11**  
 423 (2001) 057, arXiv: [hep-ph/0109064 \[hep-ph\]](https://arxiv.org/abs/hep-ph/0109064) (cit. on p. 15).
- 424

- 427 [70] X.-F. Guo and X.-N. Wang, *Multiple scattering, parton energy loss and modified fragmentation functions*  
 428 *in deeply inelastic e A scattering*, Phys. Rev. Lett. **85** (2000) 3591, arXiv: [hep-ph/0005044 \[hep-ph\]](#)  
 429 (cit. on p. 15).
- 430 [71] M. Cacciari, G. P. Salam and G. Soyez, *The Anti- $k(t)$  jet clustering algorithm*, JHEP **0804** (2008) 063,  
 431 arXiv: [0802.1189 \[hep-ph\]](#) (cit. on pp. 16, 17).
- 432 [72] S. Catani, Y. L. Dokshitzer, M. H. Seymour and B. R. Webber, *Longitudinally invariant  $K_t$  clustering*  
 433 *algorithms for hadron hadron collisions*, Nucl. Phys. **B406** (1993) 187 (cit. on p. 17).
- 434 [73] Y. L. Dokshitzer, G. D. Leder, S. Moretti and B. R. Webber, *Better jet clustering algorithms*, JHEP  
 435 **08** (1997) 001, arXiv: [hep-ph/9707323 \[hep-ph\]](#) (cit. on p. 17).
- 436 [74] G. P. Salam, *Towards Jetography*, Eur. Phys. J. **C67** (2010) 637, arXiv: [0906.1833 \[hep-ph\]](#) (cit. on  
 437 p. 17).
- 438 [75] G. P. Salam and G. Soyez, *A practical seedless infrared-safe cone jet algorithm*, Journal of High Energy  
 439 Physics **2007** (2007) 086, URL: [https://doi.org/10.1088%2F1126-6708%2F2007%2F05%2F086](https://doi.org/10.1088/2F1126-6708%2F2007%2F05%2F086)  
 440 (cit. on p. 18).
- 441 [76] ATLAS Collaboration, *Measurement of the jet radius and transverse momentum dependence of inclusive*  
 442 *jet suppression in lead–lead collisions at  $s_{NN}=2.76$  TeV with the ATLAS detector*, Physics Letters  
 443 **B 719** (2013) 220 , ISSN: 0370-2693, URL: <http://www.sciencedirect.com/science/article/pii/S037026931300049X> (cit. on p. 18).